CARBON 52 (2013) 74–82

Available at www.sciencedirect.com

SciVerse ScienceDirect

journal homepage: www.elsevier.com/locate/carbon

Controlled synthesis of Zirconium Oxide on graphene nanosheets by atomic layer deposition and its growth mechanism

Jian Liu [a], *Xiangbo Meng* [b], *Yuhai Hu* [a], *Dongsheng Geng* [a], *Mohammad Norouzi Banis* [a], *Mei Cai* [c], *Ruying Li* [a], *Xueliang Sun* [a,*]

[a] *Department of Mechanical and Materials Engineering, University of Western Ontario, London, ON, Canada N6A 5B9*
[b] *Department of Chemistry, Brookhaven National Laboratory, Upton, NY 11973, USA*
[c] *General Motors R&D Center, Warren, MI 48090-9055, USA*

ARTICLE INFO

Article history:
Received 16 June 2012
Accepted 6 September 2012
Available online 15 September 2012

ABSTRACT

Zirconium Oxide (ZrO_2) was deposited on graphene nanosheets (GNS) by atomic layer deposition (ALD) using tetrakis(dimethylamido)zirconium(IV) and water as precursors. The results indicated that both morphology and crystallinity of the deposited ZrO_2 were controllable in a temperature range of 150–250 °C. At all the temperatures studied, ZrO_2 nanoparticles were formed with lower number of ALD cycles (<10 cycles at 150 °C and <30 cycles at 200 and 250 °C), while ZrO_2 thin films were achieved uniformly with higher number of ALD cycles (>10 cycles at 150 °C and >30 cycles at 200 and 250 °C). The crystallinity of the deposited ZrO_2 was highly dependent on the deposition temperature. The ZrO_2 deposited at 150 °C exhibited mainly amorphous nature, whereas that prepared at 250 °C consisted of crystalline phase. At 200 °C, a mixture of amorphous and crystalline ZrO_2 appeared in the ZrO_2–GNS nanocomposite. In all cases, the growth of ZrO_2 on GNS showed a transformation from an "island growth" mode to a "layer-by-layer growth" mode with increasing ALD cycle. Cyclic voltammetry measurement demonstrated that 10-cycle ZrO_2–GNS nanocomposite exhibited evident electrochemical capacitance characteristics.

1. Introduction

As a two-dimensional (2D) nanostructure composed of sp^2 hybridized carbon, graphene has been drawing worldwide attention since its discovery in 2004 [1]. It possesses high thermal conductivity (~5000 $W\,m^{-1}\,K^{-1}$) [2], excellent electric conductivity (200,000 $cm^2\,V^{-1}\,s^{-1}$) [3], large surface area (theoretical valve, 2630 $m^2\,g^{-1}$) [4], and strong mechanical strength [5]. These outstanding properties promise graphene in a wide range of potential applications, such as electronics [6], supercapacitors [4], lithium ion batteries [7,8], fuel cells [9], solar cells [10,11] and bioscience/biotechnologies [12]. Recently, there is increasing interest in using graphene as a building block to fabricate multifunctional nanocomposites, which combine desired properties of each component. So far, polymer, metal, or metal oxides have been incorporated into graphene for various applications [13–20]. In particular, metal oxides supported by graphene represent one kind of nanocomposites with unique mechanical, catalytic, and electrochemical properties [15–23]. For example, TiO_2–graphene nanocomposites were used for hydrogen evolution from water photocatalytic splitting [16]. SnO_2–graphene nanocomposites showed enhanced cyclic performance and lithium storage capacity [18]. In addition, Co_3O_4 grown on graphene

* *Corresponding author:* Fax: +1 519 661 3020.
E-mail addresses: xsun@eng.uwo.ca, xsun9@uwo.ca (X. Sun).
0008-6223/$ - see front matter © 2012 Elsevier Ltd. All rights reserved.
http://dx.doi.org/10.1016/j.carbon.2012.09.007

exhibited surprisingly high catalytic activity toward oxygen reduction reaction and oxygen evolution reaction due to synergetic chemical coupling effects between Co_3O_4 and graphene [20]. Thus, metal oxide–graphene nanocomposites have great potential for applications in fuel cells, lithium ion batteries, solar cells, supercapacitors, etc.

Zirconium Oxide (ZrO_2) is an attractive material in various industrial applications due to its excellent mechanical, thermal, optical and electrical characteristics [24,25]. Up to now, there have been lots of studies on depositing ZrO_2 onto one-dimensional (1D) carbon nanotubes (CNTs) [24,25], and applying ZrO_2–CNT nanocomposites for various applications, such as catalyst supports for fuel cells [26,27], biocompatible matrix for protein immobilization [28], and transistors as advanced gate dielectrics [29]. As a young carbon nanomaterial, graphene holds several advantages over CNTs as supports for metal oxides, such as free of metallic impurities, cheap and accessible production from graphite [30]. Unfortunately, there are few efforts on developing ZrO_2–graphene nanocomposites until now. It was only recently that two literatures reported the synthesis of ZrO_2–graphene nanocomposites by an electrodeposition method, and their use for detection of organophosphorus agents and biosensor application [30,31]. Inspired by the wide applications of ZrO_2–CNTs, ZrO_2–graphene nanocomposites can also be very promising for many potential applications, which need to be fully explored. To fulfill this, it is of great importance to synthesize ZrO_2–graphene nanocomposites, especially in a controllable fashion.

In previous studies, the synthesis of ZrO_2–graphene nanocomposites was mainly achieved by electrodeposition method [30,31]. It can also be synthesized by solution-based methods, which have been widely used for the production of metal oxide–graphene nanocomposites [16–20]. Even though these methods offer the advantages of low cost and suitability for large-scale production, they are still suffering from the limitation of controlled synthesis with desired material properties. In recent years, atomic layer deposition (ALD) emerged as a powerful approach to engineering various nanostructures [32–39]. ALD is one kind of chemical vapor deposition (CVD) technique, and proceeds in a layer-by-layer manner by two sequential and self-terminating gas–solid reactions [40,41]. Compared with other kinds of CVD methods (such as plasma-enhanced CVD, conventional thermal CVD), ALD has advantages of achieving deposition of thin films with highly conformity and uniformity and precisely controlled thickness at Angstrom or monolayer level [40,41]. Moreover, the deposition temperature of ALD is usually lower than that of other CVD methods (usually <400 °C), and in some cases it can be even down to room temperature, which is beneficial for sensitive substrates [40,41]. In this study, therefore, ALD was employed to prepare ZrO_2–graphene nanocomposites, using tetrakis(dimethylamido)zirconium(IV) [$Zr(NMe_2)_4$] and H_2O as precursors, which was reported to consist of two half reactions [42]:

$$||-OH + Zr(NMe_2)_4(g) \rightarrow ||-OZr(NMe_2)_3 + C_2H_7N(g) \quad (1)$$

$$||-OZr(NMe_2)_3 + 3H_2O(g) \rightarrow ||-O-Zr-(OH)_3 + 3C_2H_7N(g) \quad (2)$$

where "||" represents substrate surface and "(g)" denotes vapor species. Homemade graphene nanosheets (GNS) were employed as substrates for ALD-ZrO_2. To our best knowledge, it is the first time of reporting the ZrO_2–GNS nanocomposites synthesized by ALD in open literatures. The deposited ZrO_2 was not only controllable in its morphology, either nanoparticles or nanofilms, but also tunable in its crystallinity, from crystalline to amorphous phase. This kind of ZrO_2–GNS nanocomposites prepared by ALD might find potential applications in many fields, such as supercapacitors, fuel cells, sensors and electronics.

2. Experimental

2.1. Preparation of GNS

GNS was prepared by thermal reduction of graphite oxide (GO) [43]. Briefly, GO was first produced by oxidizing natural graphite using a modified Hummers method [44]; then the as-synthesized GO was heated at 1050 °C for 30 s under argon gas to obtain GNS. More details about the preparation process of GNS can be found in our previous work [33,45].

2.2. ZrO_2–GNS by ALD

In a typical process, GNS powders were firstly loaded into a commercial ALD reactor (Savannah 100, Cambridge Nanotech Inc., USA) preheated to a desired temperature. A schematic diagram of the ALD reactor can be found in Fig.SI-1. Then, $Zr(NMe_2)_4$ (99%, STREM) and deionized water (H_2O) were alternatively introduced into the ALD reactor for ALD-ZrO_2. $Zr(NMe_2)_4$ was heated to 75 °C while H_2O was kept at room temperature, in order to provide sufficient vapors for ALD-ZrO_2. Delivery lines were heated to 100 °C to prevent the precursors from condensation. Nitrogen gas (99.999% in purity) was used as a carrier gas at a flow rate of 20 sccm, and the ALD reactor was maintained at a low level of base pressure (typically 0.3–0.4 Torr) by a vacuum pump (Pascal 2005 I, Adixen). One ALD cycle was executed with the completion of following six steps: (1) a 0.5 s supply of $Zr(NMe_2)_4$; (2) a 3.0 s extended exposure of $Zr(NMe_2)_4$ in the ALD reactor; (3) a 30 s purge of excess $Zr(NMe_2)_4$ and any byproducts; (4) a 1.0 s supply of H_2O (5) a 3.0 s extended exposure of H_2O in the ALD reactor; (6) a 30 s purge of excess H_2O and any byproducts. ZrO_2–GNS nanocomposites were prepared by repeating above ALD cycle at different deposition temperatures. In this study, three deposition temperatures were employed for ALD-ZrO_2 on GNS: 150, 200 and 250 °C.

2.3. Characterization of ZrO_2–GNS

The as-synthesized ZrO_2–GNS nanocomposites were characterized using a field-emission scanning electron microscope (SEM, Hitachi S4800) equipped with energy dispersive X-ray spectroscopy (EDS), transmission electron microscope (TEM, Hitachi H-7000), high-resolution TEM (HRTEM, JEOL 2010 FEG), micro X-ray diffraction (XRD, Brucker D8, Co-Kα source, λ = 1.7892 Å), and Fourier transform-infrared (FTIR, Nicolet 6700 FTIR spectrometer).

Electrochemical behaviors of the samples were evaluated with 0.5 M H_2SO_4 at room temperature using an Autolab potentiostat/galvanostat (PGSTAT-30) scanned from −0.66 to 0.24 V versus a saturated calomel reference electrode (SCE) at a scan rate of 50 mV s^{-1}.

3. Results and discussion

The pristine GNS were characterized by SEM, TEM, and FTIR, and the results are presented in Fig. 1. Fig. 1a show that the pristine GNS have an accordion-like porous structure, which is composed of many thin graphene wrinkles. TEM observation reveals that these graphene wrinkles are transparent, as seen in Fig. 1b. From FTIR spectrum in Fig. 1c, it can be seen that the pristine GNS exhibit two strong peaks located at 3450 and 1635 cm^{-1}, which correspond to stretching vibrations of hydroxyl group (–OH) and skeletal vibration of graphitic domains (C=C), respectively [45,46]. There are other two peaks observed at 1384 and 1100 cm^{-1}, which are assigned to C–OH and C–O stretching vibrations, respectively [45,46].

ZrO_2–GNS nanocomposites were prepared at 150, 200 and 250 °C with different numbers of ALD cycles. 100-cycle ZrO_2–GNS nanocomposites were characterized by SEM and XRD, and the results are shown in Fig. 2. In Fig. 2(a–c), it can be clearly seen that after 100-cycle ALD-ZrO_2, the graphene wrinkles of GNS are totally coated with smooth thin films at all three deposition temperatures. Low-magnification SEM images [Insets in Fig. 2(a–c)] indicate that these thin films are very uniformly deposited onto the whole GNS powders. The thickness of the coated wrinkles is measured to be 25 ± 0.5, 22 ± 0.7 and 19 ± 0.4 nm, for 100-cycle ZrO_2–GNS nanocomposites prepared at 150, 200 and 250 °C, respectively (Fig. 2(a–c)). Furthermore, if we suppose the pristine graphene wrinkles are about 4 nm in the thickness with a conservative estimate (as indicated in Fig. SI-2), the growth per cycle (GPC) of ALD-ZrO_2 would be roughly evaluated as 1.05, 0.90, and 0.75 nm, at 150, 200 and 250 °C, respectively. The GPC is calculated by the following equation: GPC = (thickness of coated wrinkles − thickness of pristine winkles)/(2 × cycle numbers) [33]. Fig. 2d shows the XRD results of 100-cycle ZrO_2–GNS nanocomposites prepared at 150, 200 and 250 °C. It can be seen that all samples exhibit one strong peak at 29° and one weak one at 50°, which correspond to the (022) and (100) planes of graphite (JCPDS PDF No. 08–0415), respectively. Apparently, those two peaks were induced by GNS powders. For the ZrO_2–GNS nanocomposite prepared at 250 °C, there also appear several strong peaks located at 35°, 40°, 59° and 70° in its XRD, which can be assigned to the planes of (101), (110), (112) and (211) of tetragonal ZrO_2 (JCPDS PDF No. 79–1768), respectively, or/and (111), (200), (220) and (311) of cubic ZrO_2 (JCPDS PDF No. 81–1550), respectively. These strong sharp peaks in XRD reveal the crystalline state of deposited ZrO_2 at 250 °C. With a decrease of deposition temperature, the peaks of ZrO_2 become weaker in the intensity and boarder in the half-width. Except T(101) or/and C(111) peak, the others of ZrO_2 becomes almost invisible for the ZrO_2–GNS nanocomposite prepared at 150 °C. The XRD results indicate that the crystallinity of deposited ZrO_2 experienced a gradual decrease with the decrease of deposition temperature. Based on the above results, it can be concluded that ZrO_2 thin films were successfully deposited on GNS at 150, 200 and 250 °C with 100 ALD cycles, and the GPC and crystallinity were temperature dependent.

To further understand the characteristics of ALD-ZrO_2, the morphological evolution of ALD-ZrO_2 on GNS with increasing cycle numbers was explored, and Fig. 3 presents the development of ALD-ZrO_2 on GNS after 10, 30 and 50 cycles at 150, 200 and 250 °C. At 150 °C, the graphene winkles are coated with dense ZrO_2 nanoparticles after 10 cycles (Fig. 3a). After 30 cycles, the ZrO_2 coating on the graphene winkles becomes very smooth thin films, and the thickness of the coated winkles is measured to be around 12 ± 0.5 nm, as seen in Fig. 3b. Fig. 3c indicates that 50-cycle ZrO_2 coating leads to thickness increase of the coated winkles to about 14 ± 0.7 nm, with the uniformity of ZrO_2 thin films maintained. The growth of ALD-ZrO_2 on GNS at 200 and 250 °C exhibits the similar trend of morphological evolution as that at 150 °C, as shown in Fig. 3(d–g). The deposited ZrO_2 on GNS are nanoparticles with lower ALD cycles (<10 at 150 °C and <30 at 200 and 250 °C), while thin films with higher ALD cycles (>10 at 150 °C and >30 at 200 and 250 °C). This phenomenon suggests the growth of ALD-ZrO_2 on GNS follows an "island growth" mode at the very beginning, and a "layer-by-layer growth" mode after those "islands" coalesce into thin films. From Fig. 3, one can also find that the GPC of ZrO_2 on GNS increases with the elevating temperature at the same ALD cycles. For example, with 10 cycles, the size and density of ZrO_2 nanoparticles obviously increase with the decreasing temperatures, as revealed in Fig. 3(a, d and h). Low-magnification SEM images of 10-, 30-, and 50-cycle ZrO_2–GNS nanocomposites at 150, 200 and 250 °C can be found in Fig. SI(3–5).

The morphology and structure of 10-cycle ZrO_2–GNS nanocomposites prepared at 150, 200 and 250 °C were further studied by TEM and HRTEM, and the results are presented in Fig. 4.

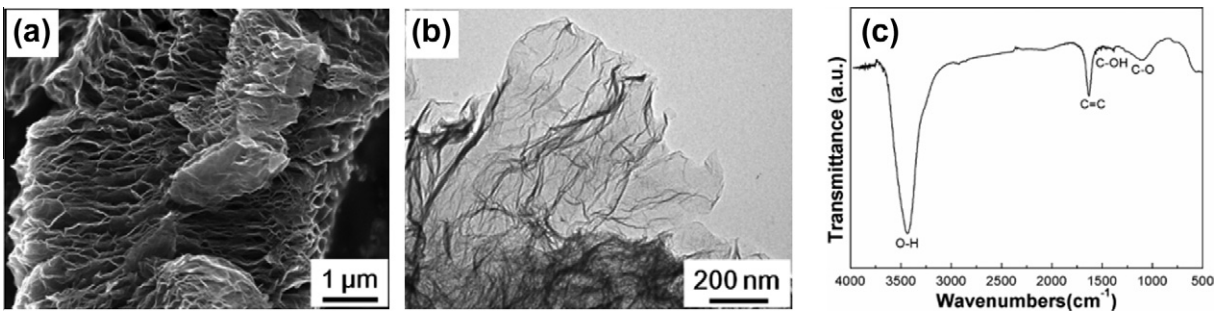

Fig. 1 – SEM image (a), TEM image (b) and FTIR spectrum (c) of the pristine GNS.

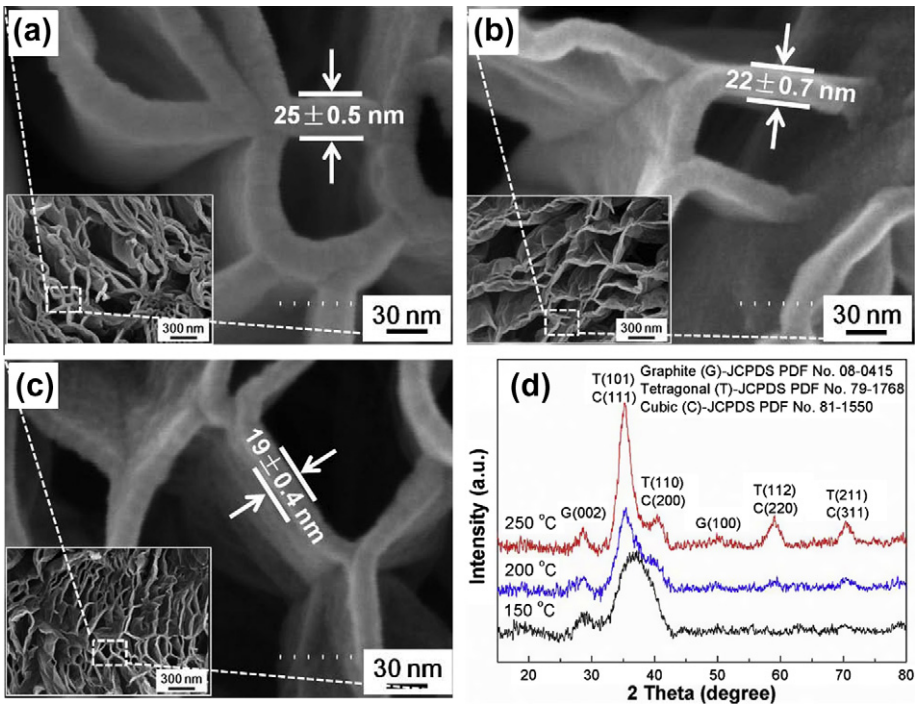

Fig. 2 – SEM images of 100-cycle ZrO_2–GNS nanocomposites prepared at (a) 150 °C, (b) 200 °C and (c) 250 °C. (d) XRD patterns of 100-cycle ZrO_2–GNS nanocomposites prepared at 150, 200 and 250 °C.

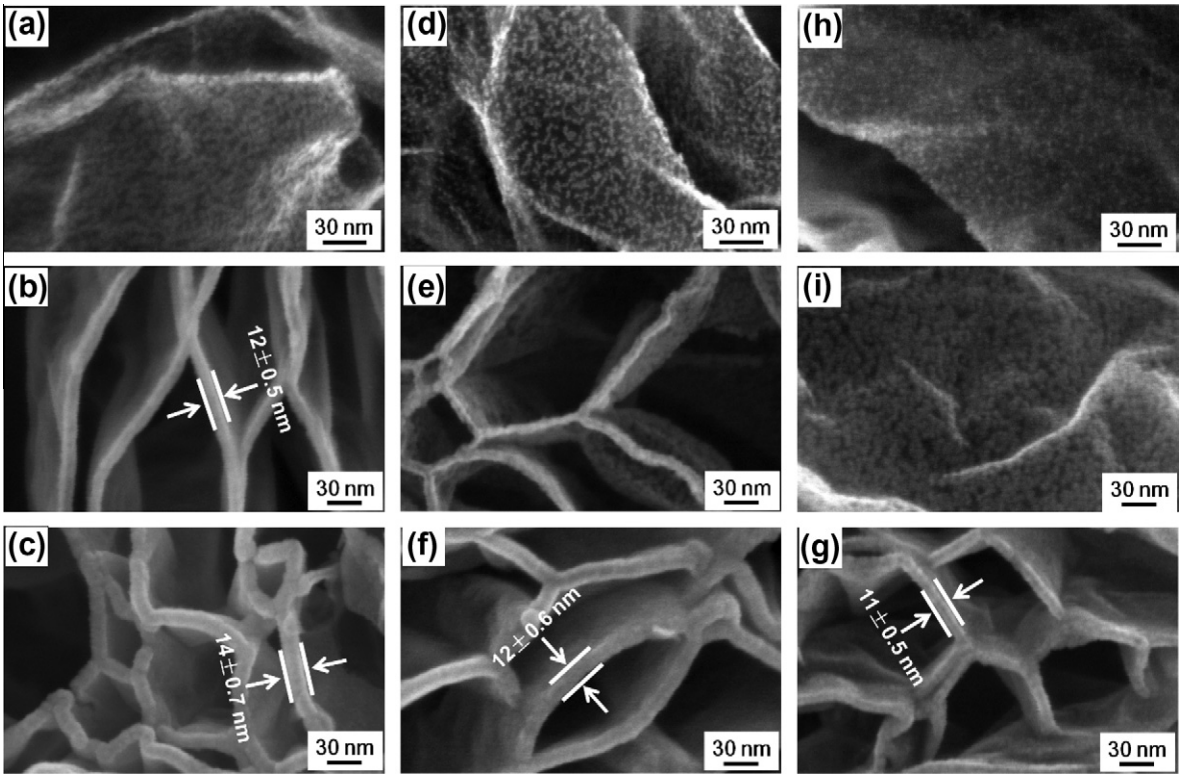

Fig. 3 – SEM images of ZrO_2–GNS nanocomposite prepared at 150 °C (a, b, c), 200 °C (d, e, f) and 250 °C (h, i, g) with 10 cycles (a, d, h), 30 cycles (b, e, i) and 50 cycles (c, f and g).

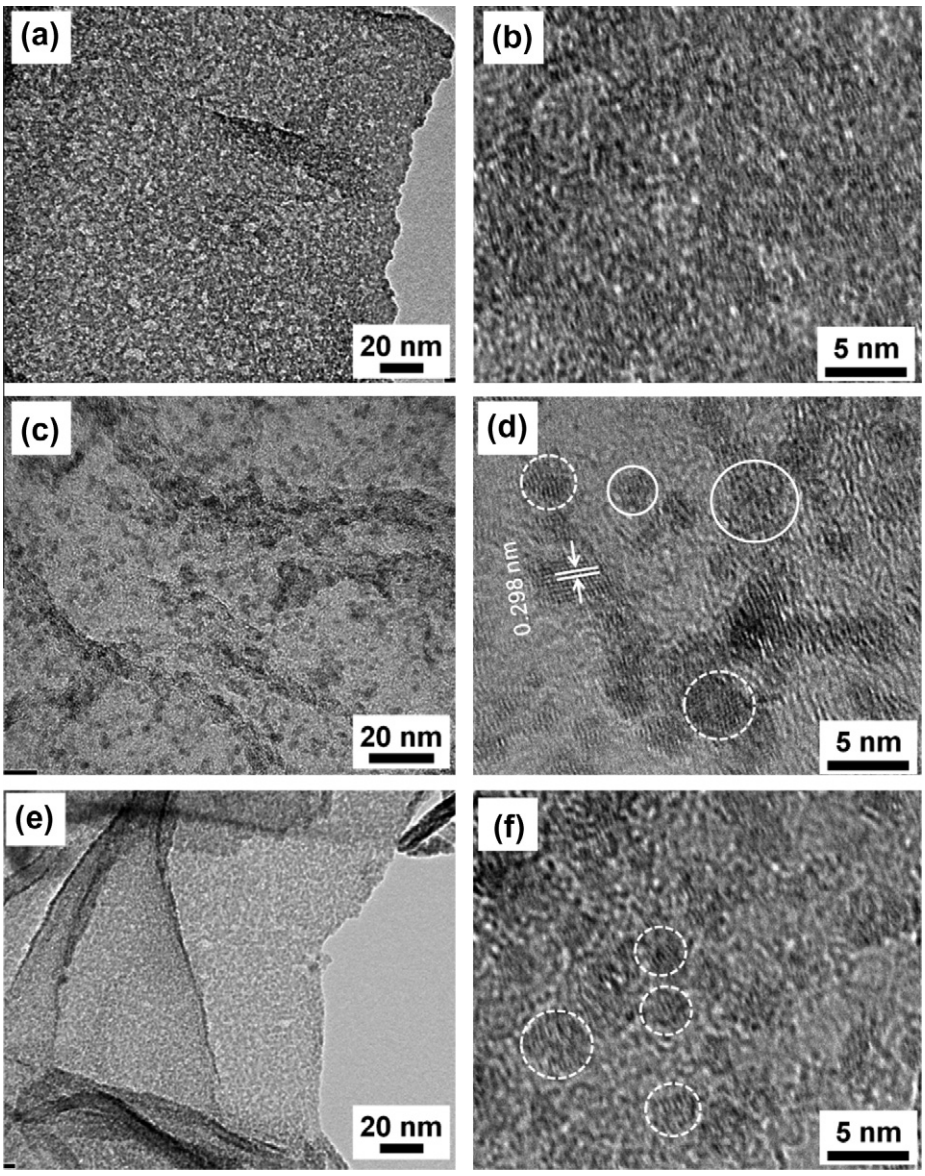

Fig. 4 – TEM (a, c, e) and HRTEM (b, d, f) images of ZrO_2–GNS nanocomposite prepared at 150 °C (a, b), 200 °C (c, d) and 250 °C (e, f) with 10 cycles.

In Fig. 4(a, c and e), one can easily find that the GNS after 10 cycles at 150, 200 and 250 °C become opaque in a large part, compared with the initial transparent GNS (Fig. 1c), indicating the deposition of dense ZrO_2 nanoparticles. The structural difference of the ZrO_2 nanoparticles among those three samples is disclosed by the HRTEM result. HRTEM image in Fig. 4b reveals the disordered nature of the deposited ZrO_2 nanoparticles at 150 °C, implying the dominance of amorphous phase in this sample. The EDS result confirms the presence of Zr and O elements in 10-cycle ZrO_2–GNS nanocomposite prepared at 150 °C (Fig. SI-6). For the sample prepared at 200 °C, the HRTEM image (Fig. 4d) indicates the coexistence of single crystalline nanoparticles (as indicated by dash circles) and amorphous ones (as marked by solid circles). The interplanar spacing of one of the single crystalline nanoparticles is measured to be 0.298 nm, agreeing well with the lattice distance between (101) planes of tetragonal ZrO_2, as seen in Fig. 4d. Fig. 4f shows the HRTEM image of 10-cycle ZrO_2–GNS nanocomposite prepared at 250 °C. Clear interplanar spaces can be observed in most of the nanoparticles in this sample (dash-circled in Fig. 4f), even though their sizes are really small (down to 1 nm), and crystalline ZrO_2 is suggested to dominate in this sample. By comparing Fig. 4b, d, and f, it can be found that the crystallinity of the deposited ZrO_2 increases with the elevating temperature. The HRTEM result is well consistent with XRD result in Fig. 2d. Based on the above studies, it can be concluded that the deposited ZrO_2 was dominated by amorphous phase at 150 °C and crystalline phase at 250 °C, and amorphous and crystalline ZrO_2 coexisted in the ZrO_2–GNS nanocomposite prepared at 200 °C.

In the following part, we will discuss the reasons responsible for the controlled morphology and crystallinity of ALD-ZrO_2 on GNS, the role of GNS as substrates for the growth of ALD materials, and propose the growth mechanism of ALD-ZrO_2 on GNS.

From the above results, it has been evidenced that the ALD-ZrO_2 on GNS were not only controllable in its morphol-

ogy, either nanoparticles or thin films, but also tunable in its crystallinity, from amorphous to crystalline. The morphology of the ALD-ZrO_2 was dependent on the ALD cycles at a given temperature, i.e. ZrO_2 nanoparticles were obtained with low ALD cycles, while ZrO_2 thin films were achieved with high ALD cycles. This phenomenon indicates that ZrO_2 followed an "island growth" mode at the early stage, while a "layer-by-layer growth" mode after the coalescence of those ZrO_2 "islands". During an ALD process, a prerequisite is the substrate surface terminated with hydroxyl groups, which serve as reactive sites for the nucleation and growth of ALD materials [40,41]. Previous studies have shown that island-growth of ALD-ZrO_2 happened on hydrogen-terminated silicon, which was lack of functional OH adsorption sites [47–49]. A recent study showed that ZnO nanoparticles could be grown on single-walled carbon nanotubes, which had a sparse amount of reactive sites for precursor chemisorptions [50]. In this work, the substrates for ALD-ZrO_2 are GNS produced by thermal reduction of GO, which usually have hydroxyl groups bonded to the carbon network [51,52]. The FTIR spectrum in Fig. 1d confirms the existence of a significant amount of hydroxyl groups on GNS, as illustrated in Fig. 5 (A1). During the first half-cycle, $Zr(NMe_2)_4$ would preferably react with –OH groups on GNS via Reaction (1), as schematically shown in Fig. 5 (A2, A3). After that, H_2O introduced in the second half-cycle would react with $Zr(NMe_2)_4$ chemically bonded on GNS through Reaction (2), generating –OH groups at the outer surface of GNS (see Fig. 5 (A4, A5)). Then the deposition of ZrO_2 would be achieved by repeating the above ALD cycle. Therefore, those hydroxyl groups dispersed on GNS would account for the island growth of ZrO_2 with low ALD cycles. With further increasing ALD cycles, those ZrO_2 'islands" would coalesce and finally close into thin films, as observed in Fig. 3. From this point on, the growth of ZrO_2 would happen in a layer-by-layer way, leading to deposition of uniform thin films. From Fig. 2 and 3, it is also obvious that with a given ALD cycle, the size of ZrO_2 particles or the thickness of ZrO_2 thin films varies with the deposition temperature. Higher deposition temperature would lead to smaller ZrO_2 particles or thinner ZrO_2 thin films. It can be explained by the temperature-dependent nature of hydroxyl groups, and high temperature could lead to dehydroxylation, as described as follows [53]:

$$2|| - OH \rightarrow || = O + H_2O \quad (3)$$

Obviously, the dehydroxylation would reduce the density of hydroxyl groups, thereby leading to the smaller ZrO_2 particles or thinner ZrO_2 thin films of ALD-ZrO_2 at a higher temperature. Besides hydroxyl groups, physisorbed $Zr(NMe_2)_4$ and H_2O are probably another reason for the higher GPC at

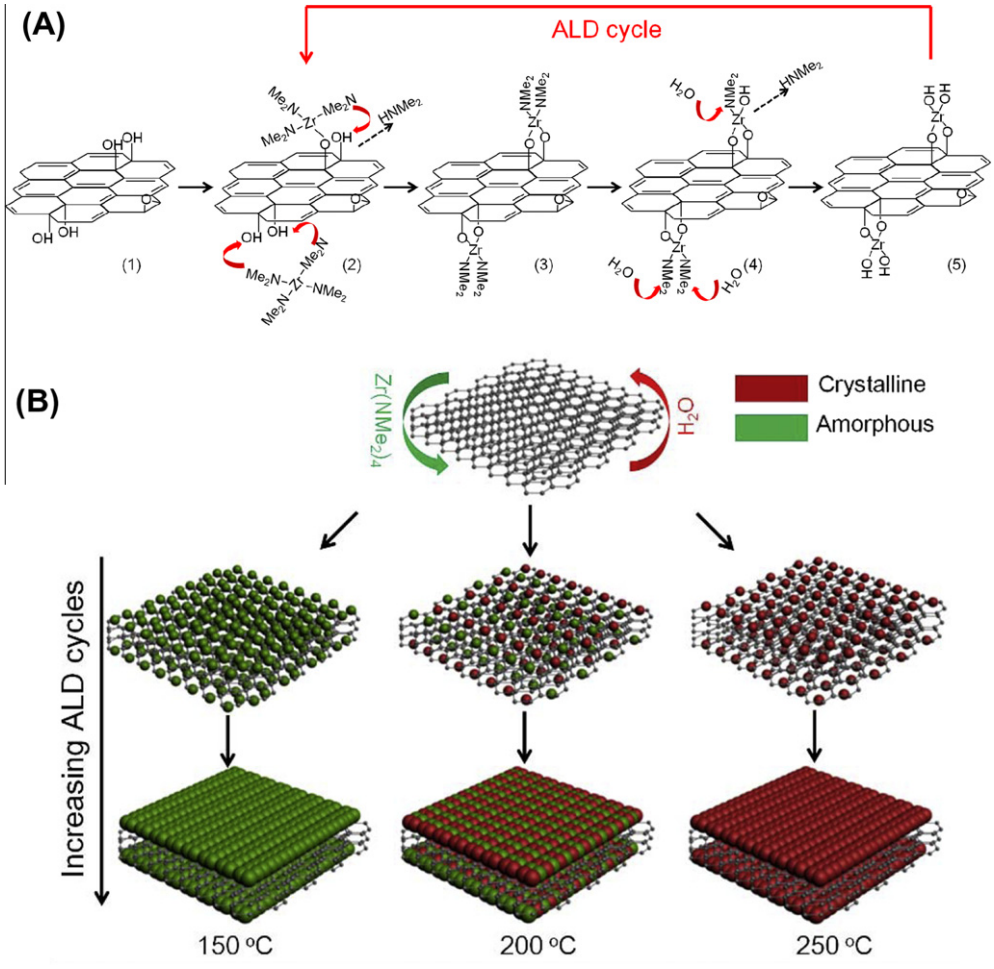

Fig. 5 – (A) Schematic diagram of one ALD cycle using $Zr(NMe_2)_4$ and H_2O as precursors [42]; (B) Schematic diagram of ZrO_2–GNS nanocomposites prepared at 150, 200 and 250 °C.

150 °C. Hausmann et al. [42] have proved that it took much longer time to purge all surface-physisorbed $Zr(NMe_2)_4$ and H_2O at lower temperatures. Therefore, given the same purge time in our case, there would be more surface-physisorbed $Zr(NMe_2)_4$ and H_2O at lower temperatures, which would in return contribute to the growth of ZrO_2. As to the crystallinity of ALD materials, previous studies have demonstrated that the temperature could affect the crystallinity of ALD materials by having influence on the reaction mechanisms [37,56], and surface mobility of absorbed species [53,55]. For $Zr(NMe_2)_4$, theoretical calculation showed that scission of metal–ligand bonds was more feasible than scission of N–C bonds [57]. Moreover, experiment study has revealed that the reaction of $Zr(NMe_2)_4$ and H_2O in ALD would follow Reaction (1) and (2) in the temperature range of 150–250 °C [42]. Therefore, it can be considered that the reaction mechanism of $Zr(NMe_2)_4$ and H_2O was not affected by the temperature change in this study. During an ALD process, high temperatures could improve the surface mobility of absorbed species and promote the ordering of the structure with minimum energy, thus leading to the growth of crystallites [54,55]. In our case, a higher temperature could enhance the mobility of absorbed species, and enable the Zr and/or O ions to occupy the positions corresponding to the lowest free energy of the crystal [55], thus resulting in the crystalline phase of ALD-ZrO_2 at 250 °C. At a given temperature, the crystallinity of ALD-ZrO_2 could be also related to the film thickness, and more crystalline ZrO_2 could be found in the thicker film [58]. The nucleation events of crystalline ZrO_2 were even during each ALD cycles. The increase of ALD cycles could result in the nucleation of more crystalline ZrO_2 and thicker film. Therefore, the thicker film might contain more crystalline ZrO_2 than the thinner film does.

From above discussion, one can see that the surface nature of GNS plays a critical role in the nucleation and growth of ALD-ZrO_2, and GNS with hydroxyl groups are desirable for this ALD process. Previous study by Dai et al. indicated that ALD-Al_2O_3 could hardly grow on pristine graphene prepared by peel-off method, due to the lack of surface functional groups [59]. Ozone pretreatment [60] and wet chemistry pretreatment [61] have been shown as effective methods to render the graphene surface more suitable to oxide precursor bonding. In this work, it is demonstrated that the as-prepared GNS by thermal reduction of GO could be directly used for the uniform deposition of ALD-ZrO_2. The functionalized GNS (Fig. 1c) could be resulted from the uncompleted reduction of GO at 1050 °C during the preparation process [45].

Fig. 5B presents a schematic diagram to summarize the ZrO_2–GNS nanocomposites prepared at different deposition temperatures. At all temperatures, ALD-ZrO_2 on GNS are nanoparticles with low ALD cycles, while thin films with high ALD cycles. The phase of deposited ZrO_2 is dominated by amorphous at 150 °C, and crystalline at 250 °C. The former two phases coexist in the ZrO_2–GNS nanocomposite prepared at 200 °C.

Recent publications have shown that ZrO_2 exhibited electrochemical capacitor performance [62,63]. Therefore, we also investigated the electrochemical capacitance behavior of the ZrO_2–GNS nanocomposite prepared by ALD in this work.

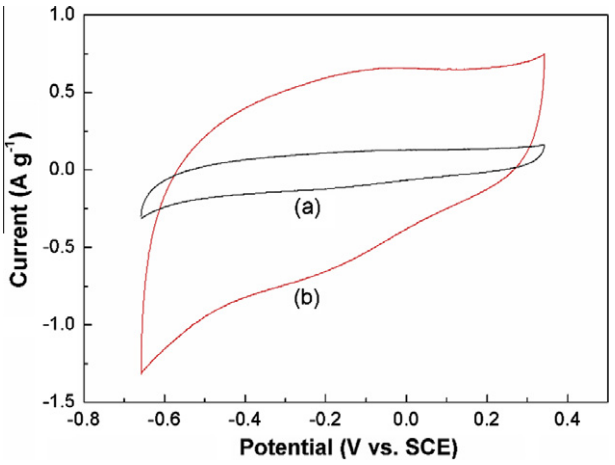

Fig. 6 – CVs of (a) GNS and (b) ZrO_2–GNS nanocomposite prepared at 250 °C with 10 cycles.

Fig. 6 shows the cyclic voltammograms (CVs) for the pristine GNS and 10-cycle ZrO_2–GNS nanocomposite prepared at 250 °C at a scan rate of 50 mV s^{-1}. The specific capacitance can be calculated from the following equation [22,23]:

$$C_m = It/\Delta V m \quad (4)$$

where C_m is the specific capacitance of the electrode (F g^{-1}), I is the charge/discharge current (A), t is the discharge time (s), ΔV is the potential window, and m is the mass of the electrode material. From Eq. (4), the area of the CV is directly proportional to the electrochemical capacitance of the electrode material. Thus, it is visually apparent from Fig. 6 that the electrochemical capacitance of 10-cycle ZrO_2–GNS nanocomposite is much higher than that of the pristine GNS. Using Eq. (4), the capacitance of the pristine GNS and 10-cycle ZrO_2–GNS is calculated to be 1.7 and 10.2 F g^{-1} at a scan rate of 50 mV s^{-1} respectively. The remarkable performance of ZrO_2–GNS nanocomposite could be attributed to the small size and high surface area of ZrO_2 nanoparticles (Fig. 3h), and the good electronic conductivity of GNS substrate. Both factors can contribute to the enhanced charge-transfer-reaction pseudocapacitance of the ZrO_2–GNS nanocomposite, which is based on fast and reversible redox reactions at the electrode surface [22]. This result implies that the ZrO_2–GNS nanocomposite prepared by ALD could be considered as promising material in the application of electrochemical capacitors. Further work is needed in order to find out the relation between the structure and the electrochemical performance of the ZrO_2–GNS nanocomposites prepared by ALD.

4. Conclusions

In this work, ZrO_2–GNS nanocomposites were prepared by ALD at deposition temperatures from 150 to 250 °C. The results showed that the crystallinity of the deposited ZrO_2 experienced a gradual decrease with the decrease of temperature. The dominant phase of the deposited ZrO_2 was crystalline at 250 °C and amorphous at 150 °C. Mixed phases of crystalline and amorphous ZrO_2 were found in the ZrO_2–GNS nanocomposite prepared at 200 °C. At all the temperatures, the ZrO_2

deposited with lower number of ALD cycles showed nanoparticle morphology, while that produced with higher number of ALD cycles exhibited as uniform thin films. In all cases, the growth of ZrO_2 on GNS followed an "island growth" mode at the early stage, and a "layer-by-layer growth" mode after the coalescence of those ZrO_2 "islands". Electrochemical capacitor evaluation indicated that 10-cycle ZrO_2–GNS nanocomposite showed specific capacitance of 10.2 F g^{-1}, which was 6 times higher than that of the pristine GNS. It is expected that this kind of ZrO_2–GNS nanocomposites, with controlled morphology and crystallinity of ZrO_2, will find potential applications in various fields, such as supercapacitors, fuel cells, batteries and electronics.

Acknowledgments

This research was supported by General Motors of Canada, Natural Sciences and Engineering Research Council of Canada (NSERC), Canada Foundation for Innovation (CFI), Ontario Research Fund (ORF), Ontario Early Researcher Award (ERA) and University of Western Ontario. The authors also would like to thank Fred Pearson at McMaster University for his help on HRTEM.

Appendix A. Supplementary data

Supplementary data associated with this article can be found, in the online version, at http://dx.doi.org/10.1016/j.carbon.2012.09.007.

REFERENCES

[1] Novoselov KS, Geim AK, Morozov SV, Jiang D, Zhang Y, Dobonos SV, et al. Electric field effect in atomically thin carbon films. Science 2004;306:666–9.
[2] Balandin AA, Ghosh S, Bao W, Calizo I, Teweldebrhan D, Miao F, et al. Superior thermal conductivity of single-layer graphene. Nano Lett 2008;8(3):902–7.
[3] Nolotin KI, Sikes KJ, Jiang Z, Klima M, Fudenberg G, Hone J, et al. Ultrahigh electron mobility in suspended graphene. Solid State Commun 2008;146:351–5.
[4] Stoller MD, Park S, Zhu Y, An J, Ruoff RS. Graphene-based ultracapacitors. Nano Lett 2008;8(10):3498–502.
[5] Lee C, Wei X, Kysar JW, Hone J. Measurement of the elastic properties and intrinsic strength of monolayer graphene. Science 2008;321:385–8.
[6] Hass J, Heer WA, Conrad EH. The growth and morphology of epitaxial multilayer graphene. J Phys: Condens Matter 2008;20:323202.
[7] Yoo E, Kim J, Hosono E, Zhou H, Kudo T, Honma I. Large reversible Li storage of graphene nanosheet families for use in rechargeable lithium ion batteries. Nano Lett 2008;8(8):2277–82.
[8] Li X, Geng D, Zhang Y, Meng X, Li R, Sun X. Superior cycle stability of nitrogen-doped graphene nanosheets as anodes for lithium ion batteries. Electrochem Commun 2011;13(8):822–5.
[9] Geng D, Chen Y, Chen Y, Li Y, Li R, Sun X, et al. High oxygen-reduction activity and durability of nitrogen-doped graphene. Energy Environ Sci 2011;4:760–4.
[10] Wang X, Zhi L, Tsao N, Tomović Ž, Li J, Müllen K. Transparent carbon films as electrodes in organic solar cells. Angew Chem Int Ed 2008;47:2990–2.
[11] Wu J, Becerril HA, Bao Z, Liu Z, Chen Y, Peumans P. Organic solar cells with solution-processed graphene transparent electrodes. Appl Phys Lett 2008;92:263302.
[12] Liu Z, Robinson JT, Sun X, Dai H. PEGylated nanographene oxide for delivery of water-insoluble cancer drugs. J Am Chem Soc 2008;130(33):10876–7.
[13] Li Y, Gao W, Ci L, Wang C, Ajayan PM. Catalytic performance of Pt nanoparticles on reduced graphene oxide for methanol electro-oxidation. Carbon 2010;48(4):1124–30.
[14] Guo S, Dong S, Wang E. Three-dimensional Pt-on-Pd bimetallic nanodendrites supported on graphene nanosheet: facile synthesis and used as an advanced nanoelectrocatalyst for methanol oxidation. ACS Nano 2010;4(1):547–55.
[15] Stankovich S, Dikin DA, Dommett GHB, Kohlhaas KM, Zimney EJ, Stach EA, et al. Graphene-based composite materials. Nature 2006;442:282–6.
[16] Zhang X, Li H, Cui X, Lin Y. Graphene/TiO_2 nanocomposites: synthesis, characterization and application in hydrogen evolution from water photocatalytic splitting. J Mater Chem 2010;20:2801–6.
[17] Wang D, Choi D, Li J, Yang Z, Nie Z, Kou R, et al. Self-assembled TiO_2–graphene hybrid nanostructures for enhanced Li-ion insertion. ACS Nano 2009;3:907–14.
[18] Paek S-M, Yoo E, Honma I. Enhanced cyclic performance and lithium storage capacity of SnO_2/graphene nanoporous electrodes with three-dimensionally delaminated flexible structure. Nano Lett 2009;9(1):72–5.
[19] Wang D, Kou R, Choi D, Yang Z, Nie Z, Li J, et al. Ternary self-assembly of ordered metal oxide–graphene nanocomposites for electrochemical energy storage. ACS Nano 2010;4(3):1587–95.
[20] Liang Y, Li Y, Wang H, Zhou J, Wang J, Regier T, et al. Co_3O_4 nanocrystals on graphene as a synergistic catalyst for oxygen reduction reaction. Nat Mater 2011;10:780–6.
[21] Huang Y, Liang J, Chen Y. An overview of the applications of graphene-based materials in supercapacitors. Small 2012;8(12):1805–34.
[22] Yu G, Hu L, Liu N, Wang H, Vosgueritchian M, Yang Y, et al. Enhancing the supercapacitor performance of graphene/MnO_2 nanostructured electrodes by conductive wrapping. Nano Lett 2011;11:4438–42.
[23] Chen S, Zhu J, Wu X, Han Q, Wang X. Graphene oxide–MnO_2 nanocomposites for supercapacitors. ACS Nano 2010;4(5):2822–30.
[24] Lu J, Zang JB, Shan SX, Huang H, Wang YH. Synthesis and characterization of core–shell structural MWNT–zirconia nanocomposites. Nano Lett 2008;8(11):4070–4.
[25] Shan Y, Gao L. Synthesis and characterization of phase controllable ZrO_2–carbon nanotube nanocomposites. Nanotechnology 2005;16:625–30.
[26] Song H, Qiu X, Li F. Promotion of carbon nanotube-supported Pt catalyst for methanol and ethanol electro-oxidation by ZrO_2 in acidic media. Appl Catal A 2009;364:1–7.
[27] Guo D, Qiu X, Zhu W, Chen L. Synthesis of sulfated ZrO_2/MWCNT composites as new supports of Pt catalysts for direct methanol fuel cell application. Appl Catal B 2009;89(3–4):597–601.
[28] Liang R, Deng M, Cui S, Chen H, Qiu J. Direct electrochemistry and electrocatalysis of myoglobin immobilized on zirconia/multi-walled carbon nanotube nanocomposite. Mater Res Bull 2010;45(12):1855–60.
[29] Javey A, Kim H, Brink M, Wang Q, Ural A, Guo J, et al. High-k dielectrics for advanced carbon-nanotube transistors and logic gates. Nature 2002;1:241–6.

[30] Du D, Liu J, Zhang X, Cui X, Lin Y. One-step electrochemical deposition of a graphene-ZrO_2 nanocomposite: preparation, characterization and application for detection of organophosphorus agents. J Mater Chem 2011;21:8032–7.
[31] Gong J, Miao X, Wan H, Song D. Facile synthesis of zirconia nanoparticles-decorated graphene hybrid nanosheets for an enzymeless methyl parathion sensor. Sens Actuators B 2012;162(1):341–7.
[32] Knez M, Nielsch K, Niinistö L. Synthesis and surface engineering of complex nanostructures by atomic layer deposition. Adv Mater 2007;19(21):3425–38.
[33] Meng X, Geng D, Liu J, Li R, Sun X. Controllable synthesis of graphene-based titanium dioxide nanocomposites by atomic layer deposition. Nanotechnology 2011;22:165602.
[34] Elam JW, Dasgupta NP, Prinz FB. ALD for clean energy conversion, utilization, and storage. MRS Bull 2011;36:899–906.
[35] Leskelä M, Ritala M, Nilsen O. Novel materials by atomic layer deposition and molecular layer deposition. MRS Bull 2011;36:877–84.
[36] Knoops HCM, Donders ME, van de Sanden MCM, Notten PHL, Kessels WMM. Atomic layer deposition for nanostructured Li-ion batteries. J Vac Sci Technol A 2012;30:010801.
[37] Meng X, Geng D, Liu J, Banis MN, Zhang Y, Li R, et al. Non-aqueous approach to synthesize amorphous/crystalline metal oxide–graphene nanosheet hybrid composites. J Phys Chem C 2010;114(43):18330–7.
[38] Elliott SD. Mechanism, products, and growth rate of atomic layer deposition of noble metals. Langmuir 2010;26(12):9179–82.
[39] Bae C, Shin H, Nielsch K. Surface modification and fabrication of 3D nanostructures by atomic layer deposition. MRS Bull 2011;36:887–97.
[40] Puurunen RL. Surface chemistry of atomic layer deposition: a case study for the trimethylaluminum/water process. J Appl Phys 2005;97:121301–52.
[41] George SM. Atomic layer deposition: an overview. Chem Rev 2010;110:111–31.
[42] Hausmann DM, Kim E, Becker J, Gordon RG. Atomic layer deposition of hafnium and Zirconium Oxides using metal amide precursors. Chem Mater 2002;14(10):4350–8.
[43] Schniepp HC, Li J-L, McAllister MJ, Sai H, Herrera-Alonso M, Adamson DH, et al. Functionalized single graphene sheets derived from splitting graphene oxide. J Phys Chem B 2006;110(17):8535–9.
[44] Hummers WS, Offeman JR. Preparation of graphitic oxide. J Am Chem Soc 1958;80(6):1339.
[45] Geng D, Yang S, Zhang Y, Yang J, Liu J, Li R, et al. Nitrogen doping effects on the structure of graphene. Appl Surf Sci 2011;257(21):9193–8.
[46] Stankovich S, Piner RD, Nguyen ST, Ruoff RS. Synthesis and exfoliation of isocyanate-treated graphene oxide nanoplatelets. Carbon 2006;44:3342–7.
[47] Puurunen RL, Vandervorst W, Besling WFA, Richard O, Bender H, Conard T, et al. Island growth in the atomic layer deposition of Zirconium Oxide and aluminum oxide on hydrogen-terminated silicon: growth mode modeling and transmission electron microscopy. J Appl Phys 2004;86:4878–89.
[48] Copel M, Gribelyuk M, Gusev E. Structure and stability of ultrathin Zirconium Oxide layer on Si(001). Appl Phys Lett 2000;76:436–8.
[49] Besling WFA, Young E, Conard T, Zhao C, Carter R, Vandervorst W, et al. Characterization of ALCVD Al_2O_3–ZrO_2 nanolaminates, link between electrical and structural properties. J Non-Cryst Solid 2002;303(1):123–33.
[50] Min YS, Lee ΠH, Lee YH, Hwang CS. Botryoidal growth of crystalline ZnO nanoparticles on a forest of single-walled carbon nanotubes by atomic layer deposition. CrystEngComm 2011;13:3451–4.
[51] Park S, Ruoff RS. Chemical methods for the production of graphenes. Nat Nanotechnol 2009;4:217–24.
[52] Li D, Müller MB, Gilje S, Kaner RB, Wallace GG. Processable aqueous dispersions of graphene nanosheets. Nat Nanotechnol 2008;13:101–5.
[53] Cassir M, Goubin F, Bernay C, Vernoux P, Lincot D. Synthesis of ZrO_2 thin films by atomic layer deposition: growth kinetics, structural and electrical properties. Appl Surf Sci 2002;193(1–4):120–8.
[54] Aarik J, Aidla A, Uustare T, Sammelselg V. Morphology and structure of TiO_2 thin films grown by atomic layer deposition. J Cryst Growth 1995;148(3):268–75.
[55] Goodman CHL, Pessa MV. Atomic layer epitaxy. J Appl Phys 1986;60:R65–81.
[56] Meng X, Zhang Y, Sun S, Li R, Sun X. Three growth modes and mechanisms for highly structure-tunable SnO_2 nanotube arrays of template-directed atomic layer deposition. J Mater Chem 2011;21:12321–30.
[57] Rodríguez-Reyes JCF, Teplyakov AV. Mechanisms of adsorption and decomposition of metal alkylamide precursors for ultrathin film growth. J Appl Phys 2008;104:084907.
[58] Hausmann DM, Gordon RG. Surface morphology and crystallinity control in the atomic layer deposition (ALD) of hafnium and Zirconium Oxide thin films. J Cryst Growth 2003;249:251–61.
[59] Wang X, Tabakman SM, Dai H. Atomic layer deposition of metal oxides on pristine and functionalized graphene. J Am Chem Soc 2008;130(26):8152–3.
[60] Lee B, Mordi G, Kim MJ, Chabal YJ, Vogel EM, Wallace RM, et al. Characteristics of high-k Al_2O_3 dielectric using ozone-based atomic layer deposition for dual-gated graphene devices. Appl Phys Lett 2010;97:043107.
[61] Garces NY, Wheeler VD, Hite JK, Jernigan GG, Tedesco JL, Nepal N, et al. Epitaxial graphene surface preparation for atomic layer deposition of Al_2O_3. J Appl Phys 2011;109:124304.
[62] Leonard KC, Suyama WE, Anderson MA. Evaluating the electrochemical capacitance of surface-charged nanoparticle oxide coatings. Langmuir 2012;28:6476–84.
[63] Nasibi M, Golozar MA, Rashed G. Nano Zirconium Oxide/carbon black as a new electrode material for electrochemical double layer capacitors. J Power Sources 2012;206:108–10.